

A NEW DIGITALLY DRIVEN PROCESS FOR THE FABRICATION OF INTEGRATED FLEX-RIGID ELECTRONICS

M. P. Shuttleworth*, M. N. Esfahani*, J. Marques-Hueso†, T. D. A. Jones†, A. Ryspayeva†,
M. P.Y. Desmulliez†, R. A. Harris* and R. W. Kay*

*Future Manufacturing Processes Research Group - School of Mechanical Engineering,
University of Leeds, LS2 9JT, UK

† Heriot-Watt University, School of Engineering & Physical Sciences, Nature Inspired
Manufacturing Centre (NIMC), Edinburgh EH14 4AS, Scotland, UK

Abstract

Conventionally, flexible and rigid electronics are produced separately using mask-based lithography techniques thus requiring connectors to join circuits together introducing potential failure modes and additional assembly. This work demonstrates a new manufacturing approach which overcomes this limitation by allowing the co-fabrication of both flex and rigid electronic circuitry within the same part. This is achieved by hybridizing polyetherimide fused filament fabrication with selective photosynthesis of silver nanoparticles and copper electroless plating. The performance and reliability of this approach has been experimentally validated via manufacturing and testing positional sensors. By printing thin layers ($< 50 \mu\text{m}$), polyetherimide exhibits a high flexibility with minimal degradation from fatigue. Where part thicknesses exceed $180 \mu\text{m}$, components start to exhibit rigid properties. A combination of various layer thicknesses allows rigid-flex substrates to be produced, with secondary processing to deposit the circuitry. Positional sensors with metalized feature sizes down to $300 \mu\text{m}$ have been fabricated that when deflected demonstrate a repeatable 1.4Ω resistance change for 43,500 cycles.

Introduction

Conventional printed circuit board (PCB) manufacturing techniques allow the economic, mass-production of high performance electronic circuits comprising of both insulator and conductor materials. These template-based fabrication methods however inhibit personalization and limit design freedoms. Research focused around additive based techniques has demonstrated major advancements for producing bespoke, multi-material, three-dimensional electronic circuits including wearable [1] and stretchable electronics [2]. Several approaches have coupled additive manufacturing techniques with Laser Direct Structuring (LDS) [3], [4] or secondary direct write (DW) processes such as ink jet printing [5], [6], aerosol jetting [7], [8] and material extrusion [9], [10]. However, further improvements are required to meet current and future requirements for electronic systems in terms of resolution, reliability and combined electrical, mechanical and thermal performance [11], [12].

Alternative approaches have used the localized synthesis of metallic nanoparticles (NPs) through light based patterning of chemically modified polyimide (PI) [13], [14] and polyetherimide (PEI) [15]. These substrates then function as a seeding site for subsequent electroless copper plating and have demonstrated the formation of highly conductive tracks with a strong adherence to the polymer. Both PEI and PI are suitable substrate materials due to their excellent heat deflection, dielectric properties, chemical stability and elastic properties. To-date these new, novel methods are confined to planer substrates of a constant thickness.

This paper presents a hybrid manufacturing method that combines additive manufacturing with selective light-based patterning of chemically modified PEI substrates. This approach allows the localized control of part thicknesses enabling flexible and rigid elements to be produced without the need for connectors. To assess the performance and durability of components produced, positional sensors were fabricated and cyclically tested with tight radii of curvature. The resultant process demonstrates highly robust devices capable of high performance operation in a range of environments.

Experimental Methods

Process Overview

The process that has been developed uses a combination of Fused Filament Fabrication (FFF), chemical modification steps, and UV treatment. This is summarized by the flowchart in Figure 2.

Substrates were made from ULTEM 1010, a PEI thermoplastic filament on a modified open source FFF 3D printer. The frame of the printer is built from aluminum extrusion and it runs on an 8-bit microcontroller using Marlin firmware. Compared to typical polymers utilized in FFF, ULTEM 1010 has a high glass transition temperature of 217 °C resulting in nozzle and print bed temperatures of 360 and 200 °C respectively. The print surface is a cast borosilicate glass sheet to ensure flatness and low thermal expansion during the build plate warm-up phase. To improve the adhesion and release characteristics of the ULTEM 1010 from the bed, a layer of Kapton® tape was applied to the glass. An example of substrate manufacture can be seen in Figure 1.

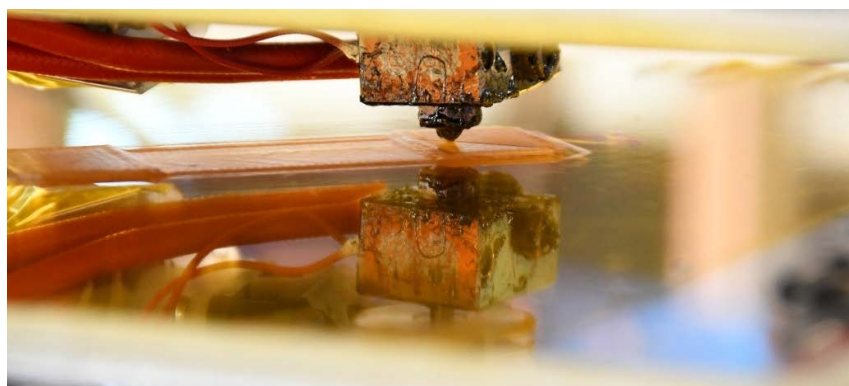


Figure 1: Printing of rigid-flex ULTEM 1010 substrates.

Following manufacture, the ULTEM substrates underwent a two-stage chemical dip to dope silver ions into the polymer chains. The first step was to crack imide rings in the ULTEM by immersion in potassium hydroxide, this break bonds which potassium ions then attach to. With the imide ring open, dipping the parts into silver nitrate displaces the potassium ions with silver ions. For patterning, components were placed into a galvo-scanning laser system with a 405 nm source, producing a spot size of 300 μm . They were then exposed to 450 $\text{J}\cdot\text{cm}^2$ from, which scanned the desired pattern. This reduced the silver ions, forming silver nanoparticles in the regions under the focal point. The residual unreacted ions are then removed through a 2 stage, acid-based ion removal wash. Between each step the samples were thoroughly washed with deionized water. With the patterning complete, the components were plated using a commercially available tartrate, electroless copper plating bath to build up the bulk conductivity of the tracks. The Cu layer thickness can be controlled by the time in the plating solution.

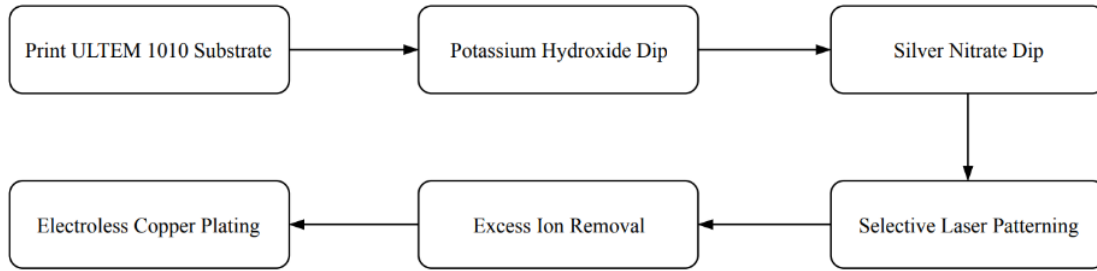


Figure 2: Generalized process flowchart for manufacturing ULTEM 1010 based electronics

Substrate Stiffness Evaluation

To evaluate how 3D printed PEI stiffness can be varied as result of selective thickness the mechanical performance of various thickness of 3D printed blank test pieces were evaluated. Thicknesses from 90 μm up to 450 μm were varied in 90 μm increments. The minimum layer height possible with this printer configuration was 45 μm with the need for at least two layers printed perpendicularly in the X-Y plane to prevent the part splitting along its infill. The true thickness of the parts was verified at 6 locations using a Mitutoyo digital micrometer with a 0.001 mm \pm 2 μm resolution. They were then loaded into a clamp before having 1 g and 2.5 g masses applied to the tip. The masses were selected to keep the deflection within the range of the laser profiler. The tip deflection was measured before and after having the loads applied using Micro-Epsilon ScanCONTROL 2900-50 laser profiler with a 4 μm z-axis resolution.

Electrical and Fatigue Performance

To determine the performance and fatigue characteristics of rigid-flex devices a positional sensor with a grid pattern like that of a standard foil type strain gauge was selected. Because of the repeated longitudinal traces this design is highly responsive under axial tension, the same loading seen on the top surface of an object being bent. The substrate consists of two rigid ends pieces connected with a 90 μm thick flexible film, printed as one piece by dynamically varying the layer heights. The first 2 layers were printed at 45 μm with subsequent layers printed at 150 μm to improve print times. The infill pattern was a rectilinear grid orientated along the length of the part, see Figure 3.

All units in mm

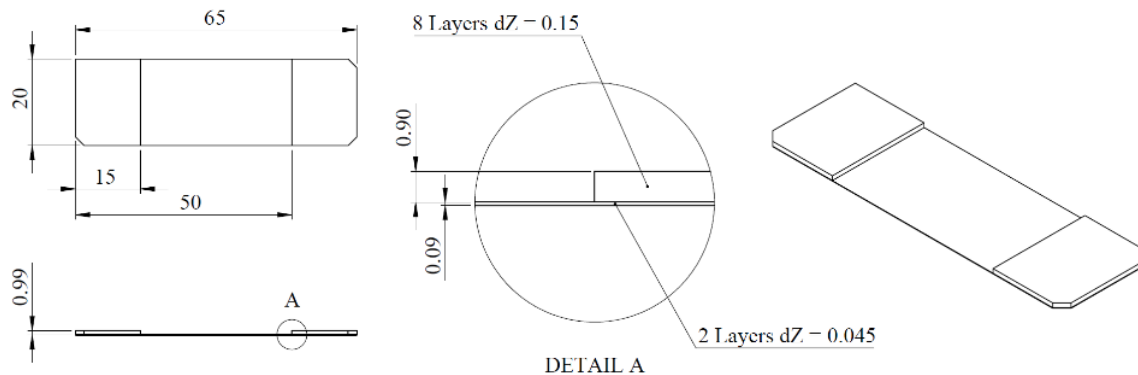


Figure 3: Schematic layout of positional sensor substrate

On the side of the substrate printed directly onto the bed, a single strain grid pattern was selectively metallized using the previously described process. The grid length was 10 mm and consisted of 32 meanders at a pitch of 500 μm which terminated at two 7 x 4 mm pads (Figure 4). The plating produced average track and gap widths of $301\pm 7\ \mu\text{m}$ and $191\pm 2\ \mu\text{m}$ respectively at the desired 500 μm pitch over 10 measurements (Figure 5). These were measured on an Olympus BX53M optical microscope at $2.5\times$ magnification using a UIS2 $5\times$ objective. The grid was positioned such that it lay in the center of the flexible region as this is the area of maximum deflection. The two pads sit on one of the rigid ends with a pair of wires were soldered onto them using lead-free solder.

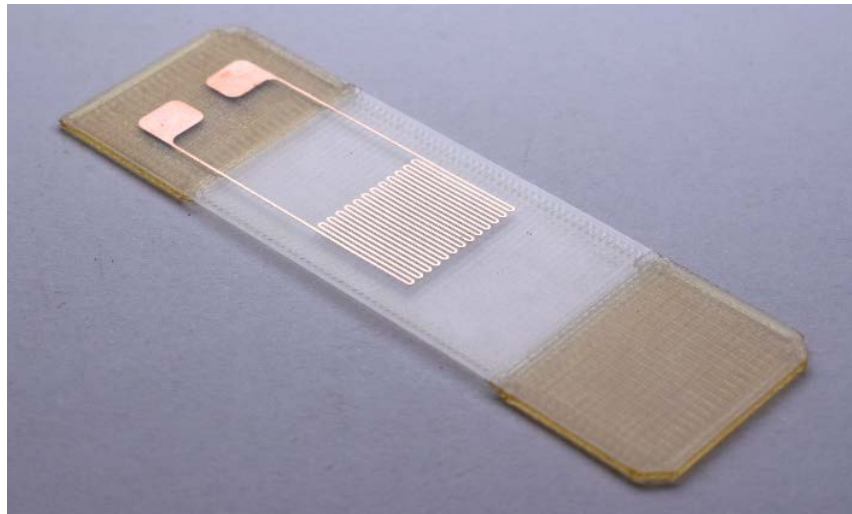


Figure 5: Plated sensor with a 10 mm grid consisting of 32 elements at a 500 μm pitch.

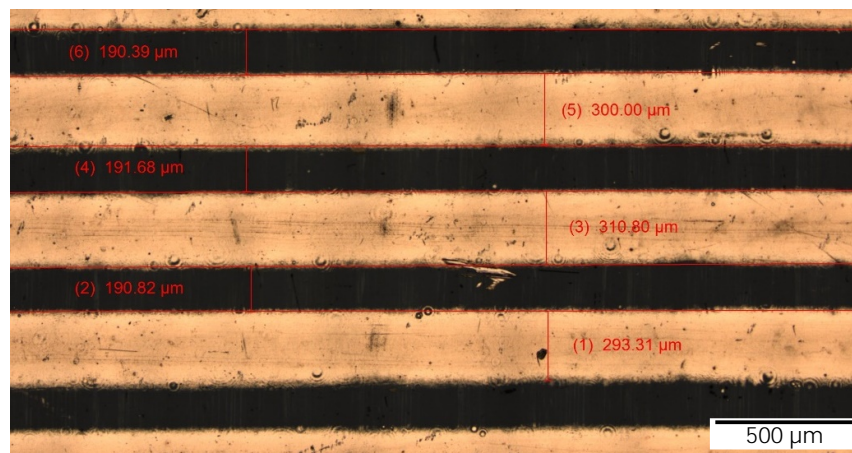


Figure 4: Optical microscope image of positional sensor grid illustrating track and gap sizes.

To test the sensors a custom linear compression rig was built that buckles the flexible region into an arc. The sensor is loaded into a set of clamps, one of which static and the other that is free to move parallel to sensor as shown in Figure 6. This is mounted on two linear rails and actuated by a stepper motor connected to a 1.5 x 8 mm leadscrew. By placing the grid in the center of the flexible region, the grid is placed in tension varying the overall resistance across the two pads with respect to bend radius. A Keithley 2450 Source Meter Unit was connected to the sensor to perform a 2-wire resistance measurement. The rig compressed each specimen 5 mm amount along its axis, stopping at evenly spaced increments to measure the resistance. Each measurement was taken 5 times at each location and then averaged before

moving to the next test point. The radius of curvature at each location was found by mounting the Micro-Epsilon laser profiler over the sensor and using a curve fitting algorithm to calculate the value.

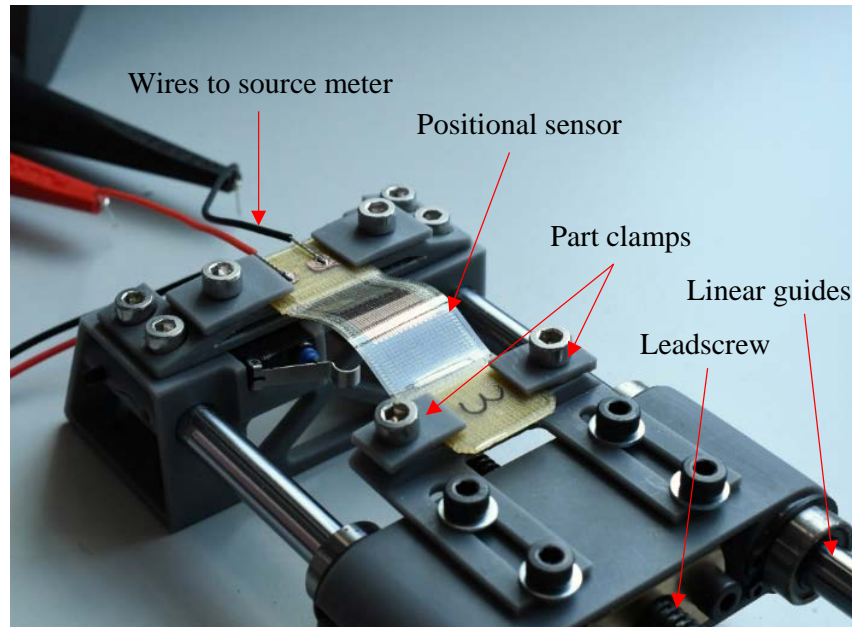


Figure 6: Positional sensor undergoing cyclic testing in the linear compression rig.

The performance of the sensors was tested by cycling each 5,000 times, compressing the samples 5 mm in total. Measurements were taken in 1.25 mm increments, including maximum and zero compression.

The fatigue test was a continuation of the performance tests, with samples being tested until electrical failure. This was defined as a spike in resistance measurements, indicating a loss of continuity, at which point the test was halted and the sensor assessed to establish the failure mode and number of cycles to failure.

Results and Discussion

Substrate Stiffness

The data from the laser profiler was compared before and after the masses were attached to establish the tip deflection due to external load. By taking the equation for stiffness: $K = F/\delta$ where K is stiffness, F is the applied load and δ is the tip deflection stiffness is then calculated. The results at 1 g and 2.5g were averaged and plotted against the true part thickness (see results in Figure 7). The plot shows a linear trend exhibiting 1.5 N.m^{-1} at $118 \mu\text{m}$ up to 116.4 N.m^{-1} at $520 \mu\text{m}$. It was observed that all test pieces printed with the $180 \mu\text{m}$ settings and above did not deflect under their own mass and were self-supporting.

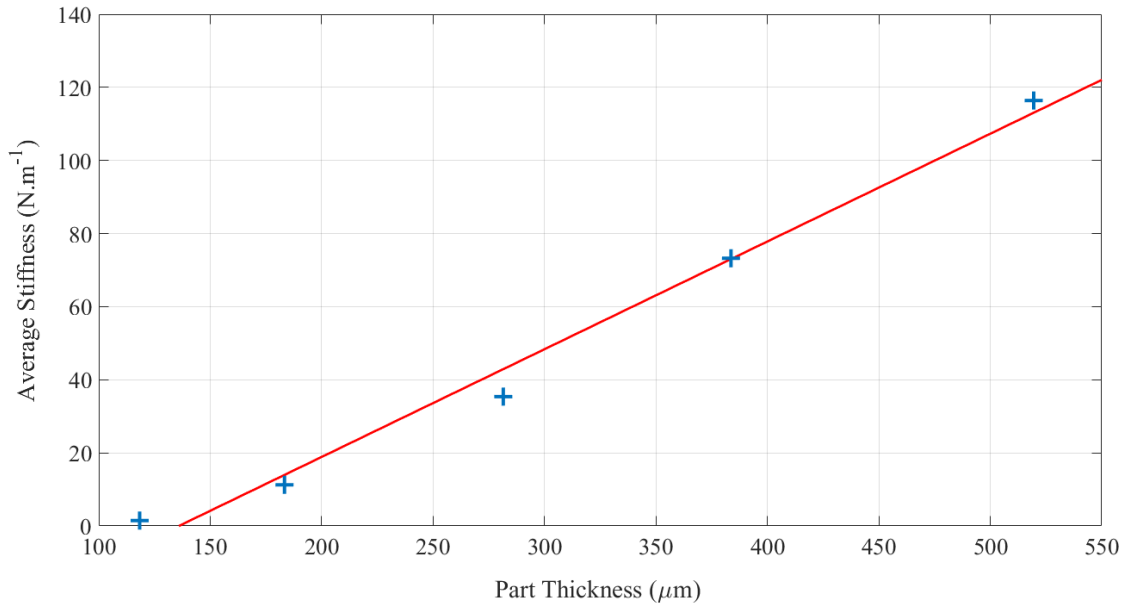


Figure 7: Graph showing average stiffness (K) vs substrates thickness.

Fatigue Test

It is accepted that copper-based sensors that rely on a change in resistance fluctuate with temperature. There are several small perturbations in the plots, however these appear consistently across all 4 positions at the same cycle count and directly correlate to environmental temperature changes in the laboratory.

To remove the effects of environmental disturbance the percentage change in resistance with respect to zero compression (dR/R_0) was plotted against the number of cycles at 4 displacements. The results of a sensor that failed after 43,500 cycles are shown in Figure 8.

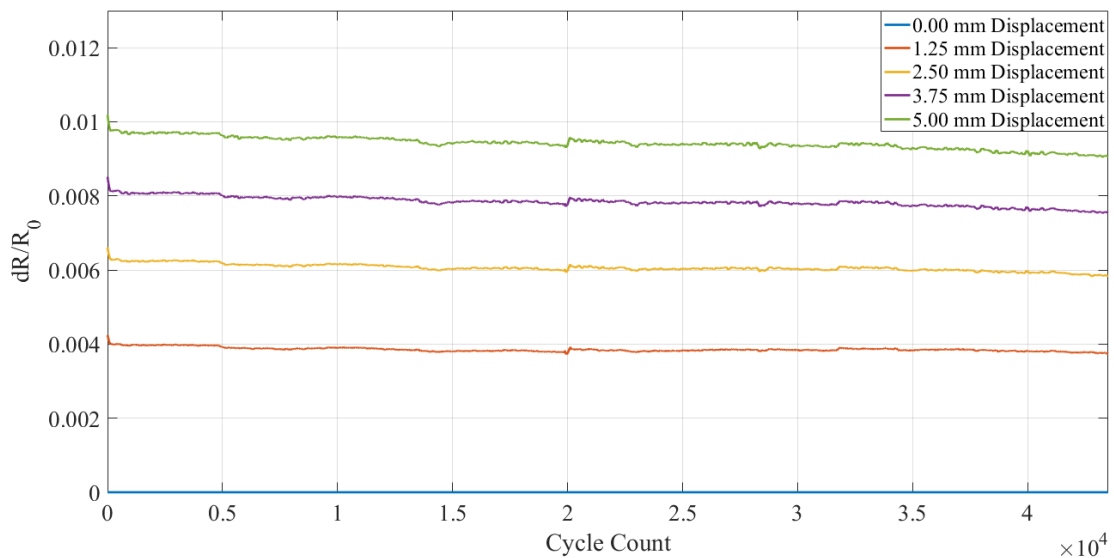


Figure 8: Graph showing variation of dR/R_0 over the lifetime of a sensor.

The first point of interest, is that the traces for all displacements are mostly flat, indicating that the performance doesn't change significantly over the lifetime of the sensor. After an initial settling period, the dR/R_0 for each line decreases by 5.2 % at 5 mm. This would suggest that over repeated, long-term cycling of the sensor will have a slight decrease in sensitivity, however will still produce repeatable and distinctly measurable outputs.

After failure the sensor was observed under an optical microscope to determine the cause of failure. In Figure 9, a crack can be seen running through both the substrate material and the copper track, creating a disconnection in the circuit, resulting in loss of data. This occurred approximately 3 mm away from the joint between flexible and rigid elements, an area that sees a high degree of curvature. Post microscopy inspection found cracks in similar positions within the substrate at the opposite end, all of which run parallel to the infill direction. After the crack was discovered, the continuity of the copper was verified using a handheld multi-meter. The test indicated that the copper was still conductive and produced resistances comparable to those seen during the test indicating that the root cause of the failure is due to the substrate fracturing which in-turn severed the electrical connection.

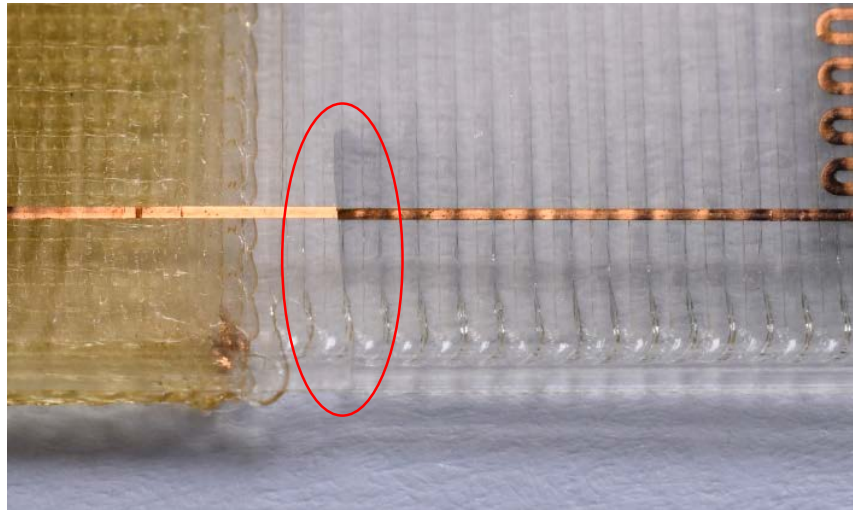


Figure 9: Close-up image of the failure point of the sensor. Note the crack running parallel to the infill direction through both substrate and copper (highlighted in red).

The devices fabricated in this study had an infill pattern that directly aligned with the deflection axis promoting crack propagation. By rotating the infill direction so that it is orientated at 45° with respect to the tracks would help to reduce or alleviate this failure mechanism due to extensive substrate cycling.

Performance test

The data indicates that a brief settling period occurs, with the output from the sensors shifts approximately 25% before becoming stable. Figure 10 shows the dR/R_0 values for a sensor for the first 200 cycles. Visible to the left of the plot is a sharp decrease, common across all displacements which flattens out after just 10 cycles without any indication that the spike has occurred. The cause of this is most likely due to the release of internal stresses in either the FFF substrates or the electroless copper plating. Because FFF relies on depositing layers of molten plastic on top of previously cooled layers, due to thermal expansion stresses build up in the printed parts. This can sometimes be seen as warping [16]. Stress in electroless depositions, can occur for multiple reasons but its occurrence is widespread and well documented [17], [18].

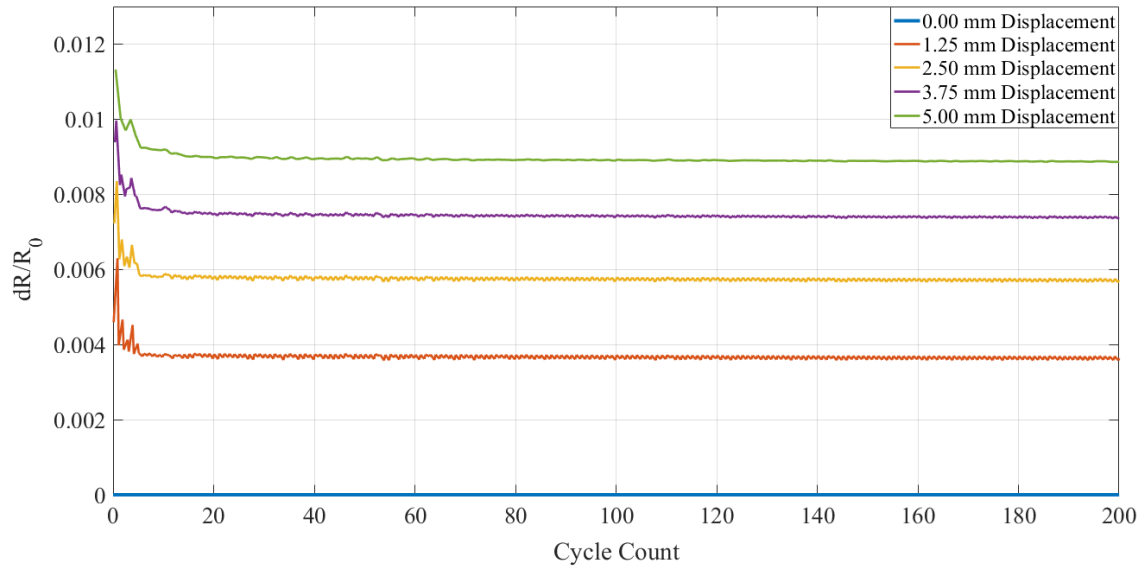


Figure 10: Graph showing variation of percentage change in resistance after 200 cycles at different compressions.

To better understand how the true resistance values changed with radius of curvature the resistance values over 4,000 cycles at different linear compressions were plotted to produce Figure 11. The various radii of curvature at the start of the test are also shown.

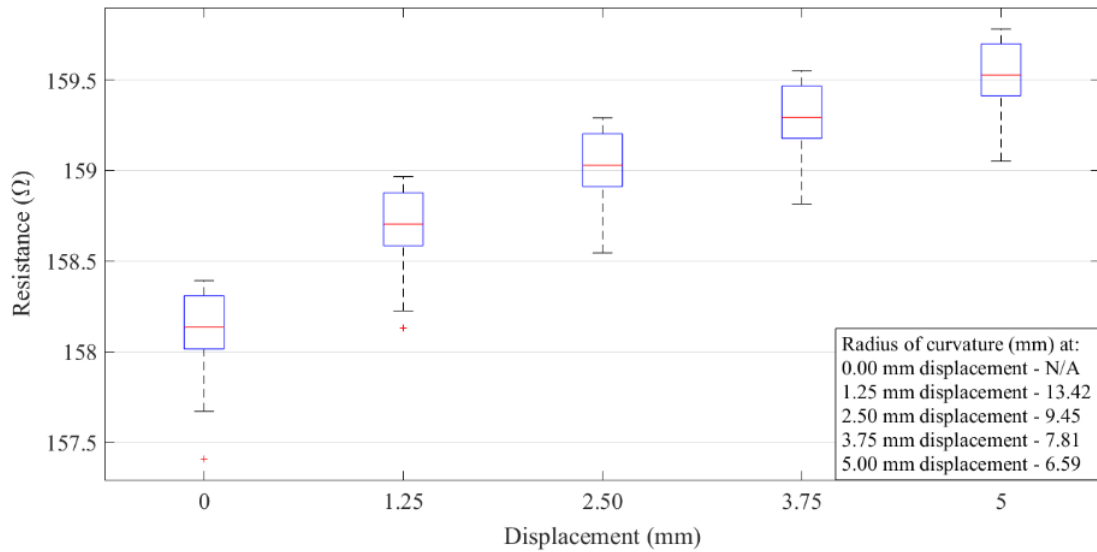


Figure 11: Boxplot comparing change resistance with linear compression over 4000 cycles.

The main visible trait is that as radius of curvature decreases due to an increase in compression, the resistance correspondingly increases. This is because of the top surface of the sensor being in tension, elongating and narrowing the copper thus shrinking its cross-sectional area and increasing its resistance. The trend also has a slight curve caused by the non-linear ratio curvature to displacement. Each plot being similar in size and shape to each other indicates

that on a cycle by cycle basis the change in resistance is consistent. This is supported by the even spacing of the lines in Figure 8 and Figure 10. By comparing the mean values, the change in resistance from 0 mm to 5 mm deflection is 1.4Ω . The maximum difference in resistances at each position is 0.75Ω however if using the value of R_0 to normalize the data on a per cycle basis this drops significantly.

Conclusions

In conclusion, a hybrid additive manufacturing process to produce highly customizable circuitry with integrated flexible elements had been demonstrated. This device performed reliably for up to 43,500 without failure however with careful optimization of the substrate design this could be extended. Moreover, after a limited settling period the conductive traces produce a consistent change in resistance with respect to deflection.

This process allows additive manufacturing to become a viable alternative for the manufacture of mass customizable, flexible, copper-based electronics with a high reliability. Potential applications range from sensory elements for soft robotics to bespoke, wearable electronics.

Acknowledgements

The authors would like to acknowledge the Engineering & Physical Sciences Research Council (EPSRC) for their financial support under the grant Photobioform II (Grant Nos. EP/N018222/1 and EP/N018265/2).

References

- [1] J. T. Muth, D. M. Vogt, R. L. Truby, Y. Mengüç, D. B. Kolesky, R. J. Wood, and J. A. Lewis, "Embedded 3D Printing of Strain Sensors within Highly Stretchable Elastomers," *Adv. Mater.*, vol. 26, no. 36, pp. 6307–6312, Sep. 2014.
- [2] K. B. Ozutemiz, J. Wissman, O. B. Ozdoganlar, and C. Majidi, "EGaIn–Metal Interfacing for Liquid Metal Circuitry and Microelectronics Integration," *Adv. Mater. Interfaces*, 2018.
- [3] B. Bachy, R. Süß-Wolf, and J. Franke, "On the quality and the accuracy of the laser direct structuring, experimental investigation and optimization," *J. Laser Appl.*, vol. 30, no. 2, p. 022006, 2018.
- [4] L. Wang, R. Suess-Wolf, M. Ulm, and J. Franke, "Investigation of the laser ablation threshold for optimizing Laser Direct Structuring in the 3D-MID technology," in *2018 International Conference on Electronics Packaging and iMAPS All Asia Conference (ICEP-IAAC)*, 2018, pp. 426–429.
- [5] J. Lessing, A. C. Glavan, S. B. Walker, C. Keplinger, J. A. Lewis, and G. M. Whitesides, "Inkjet printing of conductive inks with high lateral resolution on omniphobic 'rF paper' for paper-based electronics and MEMS," *Adv. Mater.*, vol. 26, no. 27, pp. 4677–4682, 2014.
- [6] G. McKerricher, M. Vaseem, and A. Shamim, "Fully inkjet-printed microwave passive electronics," *Microsystems Nanoeng.*, vol. 3, no. September 2016, p. 16075, 2017.

- [7] B. H. King and M. J. Renn, "Aerosol Jet® Direct Write Printing for Mil-Aero Electronic Applications," *WHITEPAPER - Optomec*, no. December, 2008.
- [8] Y.-H. Chang, K. Wang, C. Wu, Y. Chen, C. Zhang, and B. Wang, "A facile method for integrating direct-write devices into three-dimensional printed parts," *Smart Mater. Struct.*, vol. 24, no. 6, p. 065008, 2015.
- [9] J. A. Lopes, E. MacDonald, and R. B. Wicker, "Integrating stereolithography and direct print technologies for 3D structural electronics fabrication," *Rapid Prototyp. J.*, vol. 18, no. 2, pp. 129–143, 2012.
- [10] T. Wasley, J. Li, D. Ta, J. Shephard, J. Stringer, P. Smith, E. Esenturk, C. Connaughton, and R. Kay, "Additive Manufacturing of High Resolution Embedded Electronic Systems," in *Solid Freeform Fabrication 2016: Proceedings of the 26th Annual International Solid Freeform Fabrication Symposium – An Additive Manufacturing Conference*, 2016, no. November, pp. 1838–1855.
- [11] E. MacDonald, R. Salas, D. Espalin, M. Perez, E. Aguilera, D. Muse, and R. B. Wicker, "3D printing for the rapid prototyping of structural electronics," *IEEE Access*, vol. 2, pp. 234–242, 2014.
- [12] J. J. Adams, E. B. Duoss, T. F. Malkowski, M. J. Motala, B. Y. Ahn, R. G. Nuzzo, J. T. Bernhard, and J. A. Lewis, "Conformal printing of electrically small antennas on three-dimensional surfaces," *Adv. Mater.*, vol. 23, no. 11, pp. 1335–1340, 2011.
- [13] J. H. G. Ng, M. P. Y. Desmulliez, M. Lamponi, B. G. Moffat, A. C. Walker, A. McCarthy, H. Suyal, K. A. Prior, and D. P. Hand, "UV direct-writing of metals on polyimide substrates," *Proc. - 2008 2nd Electron. Syst. Technol. Conf. ESTC*, no. April, pp. 691–694, 2008.
- [14] D. Chen, Q. Lu, and Y. Zhao, "Laser-induced site-selective silver seeding on polyimide for electroless copper plating," *Appl. Surf. Sci.*, vol. 253, no. 3, pp. 1573–1580, 2006.
- [15] J. Marques-Hueso, T. D. A. Jones, D. E. Watson, A. Ryspayeva, M. N. Esfahani, M. P. Shuttleworth, R. A. Harris, R. W. Kay, and M. P. Y. Desmulliez, "A Rapid Photopatterning Method for Selective Plating of 2D and 3D Microcircuitry on Polyetherimide," *Adv. Funct. Mater.*, vol. 28, no. 6, 2018.
- [16] T. M. Wang, J. T. Xi, and Y. Jin, "A model research for prototype warp deformation in the FDM process," *Int. J. Adv. Manuf. Technol.*, vol. 33, no. 11–12, pp. 1087–1096, 2007.
- [17] S. Nakahara and Y. Okinaka, "Microstructure and Mechanical Properties of Electroless Copper Deposits," *Annu. Rev. Mater. Sci.*, vol. 21, no. 1, pp. 93–129, Aug. 1991.
- [18] Z. Wang, A. Furuya, K. Yasuda, H. Ikeda, T. Baba, M. Hagiwara, S. Toki, S. Shingubara, H. Kubota, and T. Ohmi, "Adhesion improvement of electroless copper to a polyimide film substrate by combining surface microroughening and imide ring cleavage," *J. Adhes. Sci. Technol.*, vol. 16, no. 8, pp. 1027–1040, 2002.